Check for updates

FEBS Letters

FEBS PRESS science publishing by scientists

RESEARCH ARTICLE

Structural insights into an engineered feruloyl esterase with improved MHET degrading properties

Panagiota Karampa[1], Konstantinos Makryniotis[2], Theofani-Iosifina Sousani[3], Evangelos Topakas[2], Vangelis Daskalakis[3,4] and Maria Dimarogona[1]

1 Laboratory of Structural Biology and Biotechnology, Department of Chemical Engineering, University of Patras, Greece
2 Industrial Biotechnology & Biocatalysis Group, Biotechnology Laboratory, School of Chemical Engineering, National Technical University of Athens, Greece
3 Laboratory of Biomolecular Dynamics and Engineering, Department of Chemical Engineering, University of Patras, Greece
4 Institute of Chemical Engineering Sciences (FORTH/ICE-HT), Foundation for Research and Technology Hellas, Patras, Greece

Correspondence
V. Daskalakis, Laboratory of Biomolecular Dynamics and Engineering, Department of Chemical Engineering, University of Patras, Karatheodori 1, University Campus-Rio, Patras 26504, Greece
Tel: +302610997820
E-mail: vdaskalakis@upatras.gr
and
M. Dimarogona, Laboratory of Structural Biology and Biotechnology, Department of Chemical Engineering, University of Patras, Karatheodori 1, University Campus-Rio, Patras 26504, Greece
Tel: +302610969514
E-mail: mdimarog@chemeng.upatras.gr

(Received 26 December 2025, revised 23 January 2026, accepted 10 February 2026, available online 9 March 2026)

doi:10.1002/1873-3468.70322

Edited by Christian Griesinger

Mono(2-hydroxyethyl) terephthalate (MHET) esterases (MHETases) are enzymes implicated in polyethylene terephthalate (PET) biodegradation. The present study elucidates the structural determinants that result in increased MHET degradation by a feruloyl esterase, which has been engineered to resemble the MHETase active site. The crystal structures of the variant in apo- and benzoic acid bound states reveal the changes induced by the introduced mutation, specifically the formation of a hydrogen bond and a *trans* to *cis* isomerization of a peptide bond in the vicinity of the catalytic site. Molecular dynamics simulations demonstrate the stabilization of the loop harboring the engineered residue, as well as an expansion of the substrate binding cleft, which would facilitate accommodation of a broader variety of substrates, indicative of a promiscuous biocatalyst.

Keywords: docking simulations; feruloyl esterase; G122S mutation; MHET; MHETase; molecular dynamics simulations; X-ray crystallography

Plastic accumulation in the biosphere has a severe impact on the environment and human health. As a result, intensive research efforts have lately focused on the sustainable decomposition and recycling of plastics, employing chemical, mechanical, and biological approaches. Regarding the latter, the depolymerization of polyethylene terephthalate (PET), either enzymatic or microbial, has attracted the majority of research efforts and achieved the greatest success. Enzymes known to contribute to PET degradation include PETases, which, depending on their origin, can cleave the polymeric chain to mono(2-hydroxyethyl)

Abbreviations
a.u., asymmetric unit; BA, benzoic acid; BHET, bis(2-hydroxyethyl) terephthalate; CAZy, Carbohydrate-active enzymes database; EG, ethylene glycol; FA, ferulic acid; FAE, ferulic acid esterase; *Fo*FaeC, *Fusarium oxysporum* FAE; *Fo*FaeC_G122S, *Fo*FaeC variant G122S; *Is*MHETase, *Ideonella sakaiensis* MHETase; $M(HET)_2$, a soluble methylated PET dimer; MCA, methyl caffeate; MD, molecular dynamics; MFA, methyl ferulate; MHET, mono(2-hydroxyethyl) terephthalate; MHETase, mono(2-hydroxyethyl) terephthalate esterase; M*p*CA, methyl *p*-coumarate; MT, mutant; *p*CA, *p*-coumaric acid; PCA, Principal Component Analysis; PET, polyethylene terephthalate; PETase, polyethylene terephthalate esterase; RMSD, root mean square deviation; RMSF, root mean square fluctuation; TPA, terephthalic acid; WT, wild-type.

This is an open access article under the terms of the Creative Commons Attribution-NonCommercial-NoDerivs License, which permits use and distribution in any medium, provided the original work is properly cited, the use is non-commercial and no modifications or adaptations are made.

terephthalate (MHET), ethylene glycol (EG), and terephthalic acid (TPA). Additional hydrolases, including BHETases and MHETases, hydrolyze PETase products, specifically bis(2-hydroxyethyl) terephthalate (BHET) and MHET, into TPA and EG [1,2]. While research on PETases has surged in recent years, studies on the biochemical and structural characterization of MHETases remain quite limited. Structurally, MHETases resemble tannase-like ferulic acid esterases (FAEs, EC3.1.1.73) (Fig. S1), which are enzymes that cleave the ester bond between hydroxycinnamic acids and sugars in the plant cell wall [3]. They comprise a hydrolase domain and an α-helical lid domain, stabilized by a calcium ion. Structural studies of MHETase from *Ideonella sakaiensis*, namely *Is*MHETase, in complex with PET oligomers have allowed the identification of amino acids that mediate MHET binding in the active site and the description of the MHET degradation mechanism [4–7].

*Fo*FaeC is a tannase-like FAE from *Fusarium oxysporum* that has been biochemically and structurally characterized [8,9]. It is a serine-type hydrolase, comprised of a catalytic and a lid domain with a calcium binding site, similarly to *Is*MHETase. *Fo*FaeC catalytic triad consists of Ser201, His452 and Asp412, while the amide groups of Gly123 and Thr202 form the oxyanion hole [8]. Due to its structural homology to MHETase, its potential exploitation as a plastic-degrading enzyme was investigated. Thus, an *Fo*FaeC variant, namely *Fo*FaeC_G122S, designed in order to mimic MHETase active site, was shown to exhibit improved MHET and BHET degrading activity, compared to the unmodified enzyme, without compromising its thermostability [10]. When tested on additional synthetic model substrates it was found that the variant was capable of hosting bulkier PET analogues, such as $M(HET)_2$, a soluble methylated PET dimer, in contrast to wild-type (WT). The enzyme also displayed improved catalytic properties against methyl esters of hydroxycinnamic acids, specifically methyl caffeate (MCA) and methyl *p*-coumarate (M*p*CA), while exhibiting reduced selectivity among them, in contrast to WT which preferentially cleaves methyl ferulate (MFA) [10]. Thus, it seems that mutation G122S results in a more promiscuous enzyme, without affecting its efficiency as a biocatalyst.

Here, the crystal structure of *Fo*FaeC_G122S variant is presented, in apo and benzoic acid (BA) bound state. Analysis of the determined structures highlights the introduced intramolecular interactions and structural alterations that append these improved properties to the engineered enzyme. Further docking and molecular dynamics simulations, of apo and MHET bound enzymes, corroborate the experimental findings, contributing to a better understanding of the structure–function relationships of plastic-degrading enzymes, with potential for biotechnological applications.

Materials and methods

Cloning, expression, and purification

*Fo*FaeC_G122S variant was constructed using pPICZaC vector carrying *Fo*FaeC gene (UniProt: A0A1D3S5H0). The recombinant *Fo*FaeC_G122S was expressed in *Komagataella phaffii* (syn. *Pichia pastoris*) and purified using a gravity-flow metal ion affinity chromatography column with Co^{2+} (Talon; Clontech Laboratories Inc., a Takara Bio Company, San Jose, CA, USA) as described previously [9,10]. The chromatography column was equilibrated with 20 mM Tris/HCl buffer containing 300 mM NaCl (pH 8.0). After loading the sample, it was sequentially washed with 2 column volumes (CV) of buffer, 1.5 CV of 5 mM imidazole and 1.5 CV of 10 mM imidazole in 20 mM Tris/HCl containing 300 mM NaCl (pH 8.0). The protein was eluted with three consecutive stages of 1 CV of 100 mM imidazole in the same buffer. A final polishing step was performed by size-exclusion chromatography (SEC) on a 16/60 Sephacryl column. The purity of *Fo*FaeC_G122S was checked by sodium dodecyl sulfate-polyacrylamide gel electrophoresis (SDS/PAGE) with a single band corresponding to a molecular mass of 70 kDa (Fig. S2).

Crystallization and structure determination

Purified *Fo*FaeC_G122S was concentrated to 16 $mg{\cdot}mL^{-1}$ in 20 mM Tris/HCl pH 8.0 and submitted to crystallization trials using sitting drop vapor diffusion technique. Crystallization experiments were conducted with the aid of an OryxNano crystallization robot (Douglas Instruments Ltd, East Garston, Berkshire, UK). Diffracting plate-like crystals were grown by mixing equal volumes (0.2 μL) of protein and reservoir solution (0.1 M Tris/HCl pH 8.5 and 35% (v/v) PEG400 at 20 °C). Crystals appeared after two days (Fig. S3). For cocrystallization, *Fo*FaeC_G122S and MHET were mixed at final concentrations of 15.2 $mg{\cdot}mL^{-1}$ and 10 mM, respectively, and incubated on ice for 40 min. Afterwards, crystallization was performed as described above, mixing 0.4 μL protein-MHET solution and 0.2 μL reservoir solution. Crystals appeared within 2 days in the presence of 0.1 M Tris/HCl pH 8.5, 37% (v/v) PEG400.

For X-ray data collection, crystals were mounted on litholoops and flash cooled in liquid N_2. X-ray diffraction data were collected at beamline P13, operated by EMBL Hamburg at the PETRA III storage ring (DESY, Hamburg, Germany) [11]. *Fo*FaeC_G122S and MHET-*Fo*FaeC_G122S crystals diffracted to 1.90 Å and 1.71 Å, respectively. Both crystals were grown in space group $P2_1$

18733468, 2026, 18, Downloaded from https://febs.onlinelibrary.wiley.com/doi/10.1002/1873-3468.70322 by DESY - Zentralbibliothek, Wiley Online Library on [07/10/2026]. See the Terms and Conditions (https://onlinelibrary.wiley.com/terms-and-conditions) on Wiley Online Library for rules of use; OA articles are governed by the applicable Creative Commons License

with 2 molecules in the asymmetric unit. The resulting datasets were processed using *XDS* [12], and the data integration and scaling were performed with *AIMLESS* [13] at the *CCP4i2* program suite [14]. Both crystal structures were determined by molecular replacement with *PHASER* [15] using the apo structure of *Fo*FaeC as the starting model (PDB code: 6FAT). Iterative rounds of manual model building and refinement of the structure were also performed using *COOT* [16] and *REFMAC5* [17], respectively. The atomic coordinates and structure factors for crystal structures of *Fo*FaeC_G122S and *Fo*FaeC_G122S in complex with BA have been deposited in the Protein Data Bank (PDB; https://www.rcsb.org/) under accession codes 9I50 and 9HUN, respectively.

Molecular dynamics (MD) simulations and analysis

The initial coordinates were taken from the *Fo*FaeC crystal structure (PDB code: 6FAT, chain: B) for the wild-type (WT) and *Fo*FaeC_G122S (PDB code: 9I50, chain: B) for the mutant (MT). Glycosylations and other ligands were removed prior to the preparation of the systems; otherwise, all resolved water molecules were retained in the structures. The protonation states of Glu and Asp residues were predicted by *PROPKA* method [18,19] in the *PDB2QR* server (https://server.poissonboltzmann.org/) at pH 6.0, corresponding to the reported optimum pH for *Fo*FaeC activity [20]. The assigned protonation states were further validated by visual inspection to preserve the local geometry of the respective residues, as described in the resolved proteins and to ensure an optimum hydrogen bonding network. Histidine protonation states were also assigned based on visual inspection of their local environment to ensure an optimum hydrogen bonding network that reproduces the proper local geometry, as determined within the resolved structures. The catalytic His452 was protonated in accordance with the proposed protonation state of the catalytic His528 found in the homolog *Is*MHETase, in a previous study [5]. In detail, all His residues were protonated only at the N_ε sites, except His73, His174, His192, His252, and His452 that were protonated only at the N_δ sites. Asp367, Glu210, and Glu346 were kept always protonated, whereas all other acidic residues were left deprotonated. The model structures were embedded in a $12 \times 12 \times 12$ nm^3 simulation box-cell and hydrated by around 55 000 TIP3P water molecules [21]. Each system was neutralized by adding 5 chloride anions (Cl^-) (~173 k atoms in total/system). To be consistent with the crystallographic conditions, no additional salt ions were added. The Charmm36 Force Field [22] was employed for the description of the polypeptide chains and ions.

Based on published protocols, all models were relaxed and equilibrated with gradual removal of constraints on the protein backbone-heavy atoms [23]. Briefly, a series of constant volume (nVT) and constant pressure (nPT) ensemble runs increased the temperature from 100 K to 308 K over 50 ns prior to production runs. Classical MD simulations were run for 500 ns in four independent trajectories per system (WT and MT) with variant initial coordinates-velocities derived from the last step of equilibration (1 ns apart). Newton's equations of motion were integrated with a time step of 2.0 fs. The leapfrog integrator in *GROMACS 2022.5* was employed [24]. The production runs have been performed in the constant pressure nPT ensemble with isotropic coupling (compressibility at 4.5×10^{-5}). Moreover, the Van der Waals interactions were smoothly truncated between 1.0 and 1.2 nm with the Verlet cutoff scheme (force-switch algorithm and tolerance at 10^{-3}). Short-range electrostatic interactions were truncated at 1.2 nm and long-range contributions were computed within the Particle-Mesh-Ewald (PME) approximation with tolerance at 10^{-5} and Fourier spacing at 0.15 [25]. All hydrogen-heavy atom bond lengths were constrained after equilibration employing the LINCS algorithm [26]. For the production, the v-rescale thermostat is employed [27] (temperature coupling constant = 0.5) and the C-rescale barostat [28] (1 atm; pressure coupling constant = 2.0). The first 100 ns of each trajectory were considered as further equilibration time and were disregarded from the analysis. In total, the production sampling time of these two systems with four trajectories/system running for 0.5 μs each is 4 μs.

For the analysis, principal component analysis (PCA) and k-means clustering were performed by in-house scripts based on the sklearn python library. The root-mean-square fluctuation (RMSF) and B-factors were calculated for the protein alpha carbon (Cα) atoms and weight-averaged based on the eigenvalues of the three main PCA components per trajectory that represent 35–40% of the total motion sampled per replicate trajectory. Four clusters were identified per system (WT and MT) by the k-means algorithm (Figs S4 and S5, respectively), and the representative structure from each cluster was extracted for docking simulations.

Molecular docking of MHET

Docking analysis was performed using *YASARA 21.6.17* software [29]. The key conformations for *Fo*FaeC and *Fo*FaeC_G122S obtained from the MD analysis (k-means clustering) were used as initial coordinates for docking. Water molecules were removed, and energy minimization of all structures was held in *YASARA*, without compromising the identity of the predicted key conformations. MHET was built as follows: a nonhydrolysable form of MHET, named MHETA, captured at the catalytic center of a MHETase was downloaded from PDBe (PDB code: 6QGA) [6] and the nitrogen atom was substituted by oxygen to build the ester bond using *YASARA*. The ligand was placed in the active site of each structure by aligning

18733468, 2026, 18, Downloaded from https://febs.onlinelibrary.wiley.com/doi/10.1002/1873-3468.70322 by DESY - Zentralbibliothek, Wiley Online Library on [07/10/2026]. See the Terms and Conditions (https://onlinelibrary.wiley.com/terms-and-conditions) on Wiley Online Library for rules of use; OA articles are governed by the applicable Creative Commons License

with MHETase using *MUSTANG* [30] and the resulting structures were submitted to perform local docking in *YASARA*. Structures obtained from docking analysis were ordered based on their binding free energy and predicted dissociation constant (K_d). The docked structure with the most favorable energy and the lowest K_d of each enzyme was selected for further MD simulations, with the constraint that the distance between the hydroxyl group of the catalytic serine (Ser201) and the carbon atom of the carbonyl group connected to the ethylene glycol moiety of MHET did not exceed 4 Å. *CHARMM-GUI* [31,32] was used to construct the compatible parameter files of MHET for Charmm36 Force Field. Classical MD simulations were run for 500 ns in four independent trajectories per complex system (WT and MT), as in the apo structures.

Thermostability

Thermodynamic stability of both *Fo*FaeC and *Fo*FaeC_G122S enzymes was checked through essays at 308, 328, and 348 K. Initial coordinates of each system were taken from the last frame (t = 500 ns) of the apo MD simulations at 308 K. The structures were heated to the goal temperature using a 10 ns simulation. Then, the classical MD simulations for each system were run for 100 ns saving the system snapshots every 10 ps.

For the analysis, the dimensionless parameter (Λ) was used, describing the dependence of the squared generalized order parameters (S^2) for the backbone N-H bond vectors on the temperature [33,34]. The first residue (Asp36) and all prolines were excluded from the calculation, as Asp36 is charged due to the appearance of three hydrogen atoms connected to the N and prolines lack the presence of a hydrogen atom to the nitrogen. The Λ values were determined providing thus information about the temperature dependent fluctuations of N-H bond vectors. Lower Λ values indicate a more thermostable protein molecule.

Results and discussion

Crystal structure of FoFaeC_G122S

The crystal structure of *Fo*FaeC_G122S was determined to a resolution of 1.90 Å, in apo form (PDB code: 9I50), and to 1.71 Å, in complex with BA (PDB code: 9HUN). Data collection and refinement statistics are shown in Tables S1 and S2. Similarly to the unmodified enzyme, *Fo*FaeC_G122S crystallized in space group $P2_1$ with 2 molecules in the asymmetric unit (a.u.). It is composed of an α/β hydrolase domain, and an α-helical lid domain composed of residues 229–389 (Fig. 1A). The post-translational modifications observed in the WT enzyme are also present in the modified one. Specifically, N-linked glycans at residues 66, 101, 111, 151, and 362, as well as the six disulfide bonds between cysteines 41–88, 76–127, 200–453, 269–287, 296–304, and 516–538 are identified. The Cys200-Cys453 disulfide bond is partially broken, likely due to the radiation damage. In its reduced state, Cys200 forms hydrogen bonds with three water molecules, one of which also interacts with the hydroxyl group of the engineered Ser122 (Fig. 1B). The lid domain is stabilized by a calcium ion that is coordinated by seven oxygen atoms in each monomer, as in the WT.

Superposition of chain B of WT (PDB code: 6FAT) and *Fo*FaeC_G122S structures over all atoms indicates an RMSD of 0.248 Å. In agreement with that, visual inspection of the superimposed structures does not indicate significant structural alterations. The most evident change induced by the engineered amino acid is the formation of three hydrogen bonds. Two of these involve interactions between Ser122 and Gln129, in which the side chain hydroxyl group and the backbone amide of engineered Ser122 form hydrogen bonds with the side chain carbonyl group of Gln129, inducing a shift of its C_d atom by 0.3 Å toward Ser122 (Fig. 1C). The third hydrogen bond is formed between the NE2 atom of Gln129 and the carboxyl group of Asp132. In contrast, in the unmodified enzyme, Gln129 interacts only with 2 neighboring water molecules that are also conserved in *Fo*FaeC_G122S. In addition to that, the peptide bond between Ala125 and Gly126 adopts a twisted *trans* conformation in molecule A and a *cis* conformation in molecule B of *Fo*FaeC_G122S, in contrast to the wild-type enzyme, where this bond adopts a *trans* conformation in both monomers in the asymmetric unit. This *cis* conformation is accompanied by a 'closed' conformation of Phe342, pointing toward the putative ligand binding site (Fig. 1D). This alteration results in the formation of a hydrogen bond between the carbonyl oxygen of Ala125 and atom ND2 of Asn148.

Crystal structure of FoFaeC_G122S in complex with benzoic acid

The *Fo*FaeC_G122S-benzoic acid (BA) complex structure reveals a set of noncovalent interactions mediating the binding of the ligand (Fig. 2A). Specifically, the benzoic carboxyl group forms hydrogen bonds with the hydroxyl group of one of the two rotameric configurations of the catalytic Ser, the side chain hydroxyl and the backbone amide of Thr202, and the backbone amide of Gly123 (Fig. 2B). The two latter amino acids form the oxyanion hole said to stabilize the tetrahedral intermediate [5]. Regarding the side chain of the catalytic Ser, while in the apo form of *Fo*FaeC_G122S it only appears in the t rotameric form, in the BA bound

18733468, 2026, 18, Downloaded from https://febs.onlinelibrary.wiley.com/doi/10.1002/1873-3468.70322 by DESY - Zentralbibliothek, Wiley Online Library on [07/10/2026]. See the Terms and Conditions (https://onlinelibrary.wiley.com/terms-and-conditions) on Wiley Online Library for rules of use; OA articles are governed by the applicable Creative Commons License

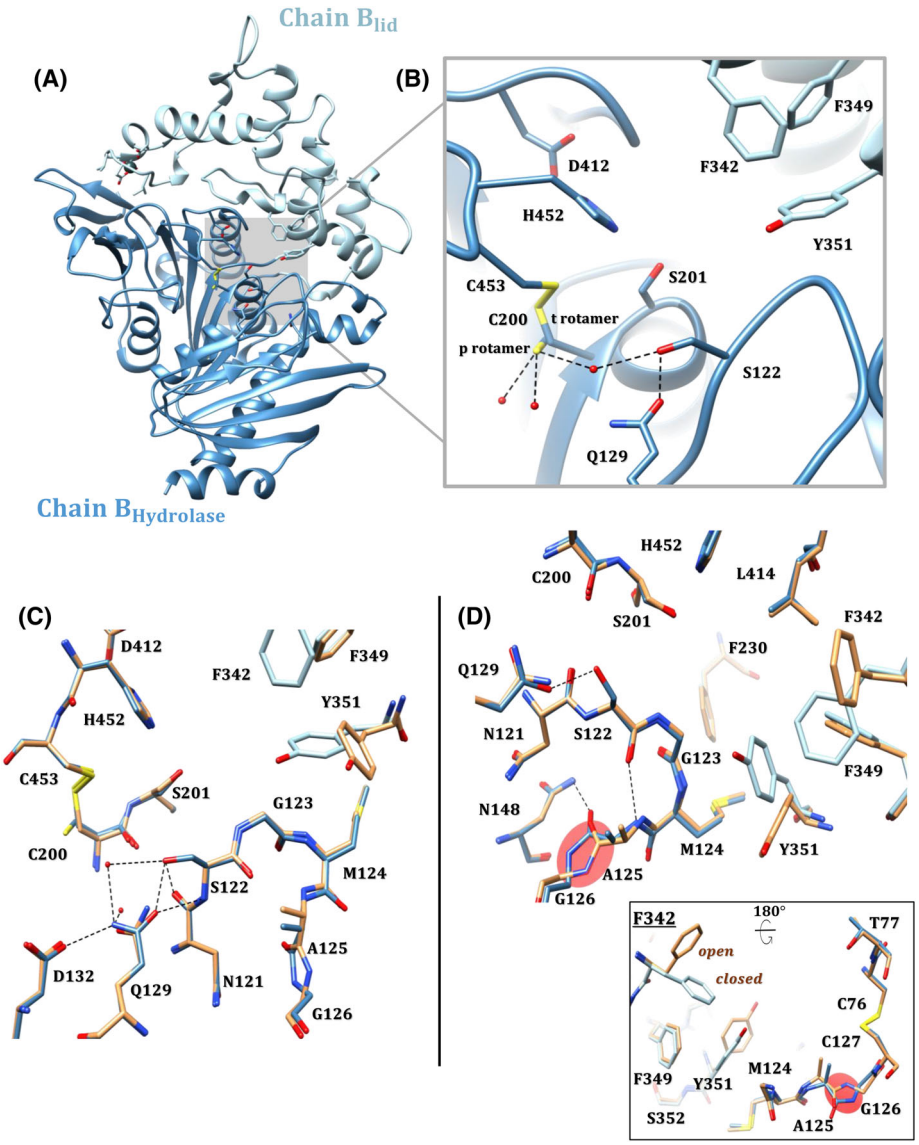


Fig. 1. Crystal structure of *Fo*FaeC_G122S. (A) Cartoon representation of *Fo*FaeC_G122S monomer (molecule B). Lid domain (residues 229–389) is represented in light blue, while the hydrolase domain is in steel blue. Calcium ion is shown in dark gray sphere. (B) The two rotamers of Cys200 that participate in disulfide bond formation are shown. The reduced form of Cys200 forms hydrogen bonds (depicted in dashed black lines) with three water molecules (red spheres). Amino acids are shown as sticks, while oxygen and nitrogen atoms are shown in red and blue, respectively. (C) Stick representation of *Fo*FaeC_G122S superimposed on the wild-type *Fo*FaeC (PDB code: 6FAT, molecule B). Close-up view of the mutation region of *Fo*FaeC_G122S, with hydrogen bonds formed between the engineered Ser122 and Gln129, as well as between Gln129 and Asp132. (D) Stick representation of the cis/trans conformation between Ala125 – Gly126, highlighting the closed/open conformation of Phe342. The hydrogen bonds shown in dashed black lines correspond to the *Fo*FaeC_G122S structure.

structure, it is in both t and p rotameric forms [35], which results in its Oγ atom being 2.40 Å and 3.49 Å from the carboxyl oxygen of BA, respectively (Fig. 2B). The p rotamer is stabilized through a hydrogen bond with the hydroxyl group of engineered Ser122, and is not observed in the *p*-coumaric bound structure of *Fo*FaeC WT, where an m rotameric form appears (Fig. 2C). The aromatic ring of BA is stabilized via T-shaped π-π interactions with Tyr351, in a hydrophobic environment created by Phe230, Phe349, Phe342, Leu414, and Ile415 (Fig. 2B). The *cis* conformation of the peptide bond between Ala125 and Gly126 is observed in both molecules of the a.u., similarly to monomer B of 'apo' *Fo*FaeC_G122S and both

18733468, 2026, 18, Downloaded from https://febs.onlinelibrary.wiley.com/doi/10.1002/1873-3468.70322 by DESY - Zentralbibliothek, Wiley Online Library on [07/10/2026]. See the Terms and Conditions (https://onlinelibrary.wiley.com/terms-and-conditions) on Wiley Online Library for rules of use; OA articles are governed by the applicable Creative Commons License

monomers of *Fo*FaeC in complex with *p*-coumaric acid (*p*CA) (PDB code: 8BHH) [9]. In addition, in both monomers, Phe342 adopts an inward conformation. This phenylalanine placement, which appears in tandem with the *cis* Ala125-Gly126 bond, is only observed in substrate-bound structures of the enzyme, as well as molecule B of apo *Fo*FaeC_G122S, as described above. It should be mentioned that unmodeled electron density at the active site of monomer B indicates the occurrence of an unidentified ligand (Fig. S6), probably originating from the crystallization solution, other than water, that could influence the configuration of amino acids forming the binding cleft. Regarding Tyr351, which has been previously shown to change conformation upon substrate binding, and whose mobility upon substrate binding as Phe415 in *Is*MHETase has also been previously demonstrated [6], it does not seem to change conformation between the apo and BA bound state. Still, electron density indicates increased mobility of this amino acid (Fig. S7), further confirmed by its relatively increased B-factors, also observed in the neighboring Pro350 and Phe349. Compared to the *p*CA bound *Fo*FaeC WT structure, the aromatic rings of the two ligands occupy nearly identical positions, with their C1 carbons overlapping. However, the C4 carbon is rotated by approximately 33° around an axis perpendicular to the ring plane and passes through C1 of the benzene ring (Fig. 2C).

In conclusion, considering also our previous results on *Fo*FaeC apo and *p*CA bound structures, even though Tyr351 displays considerable mobility, the most evident structural rearrangement upon substrate binding includes Phe342 which seems to be implicated to the substrate placement into the active site (Fig. 2B) and the adoption of *cis* conformation in the peptide bond connecting residues 125 and 126. The distance between Phe342-BA centroids is 7.7 Å (Fig. 2B), which could not imply a direct π-π interaction [36].

Comparison with BA bound IsMHETase structure

Currently, there are two crystal structures of *I. sakaiensis* MHETase in complex with BA (PDB codes: 6QGB, 6QZ3), both with BA orientation almost opposite to *Fo*FaeC_G122S-BA structure (Fig. 3A). This position arises from the ionic interaction between the carboxylate group of BA and the positively charged Arg411 in *Is*MHETase, which is not conserved in *Fo*FaeC. The importance of Arg411 for TPA recognition via its positive charge has been demonstrated in previous experimental and computational studies [6,37]. In *Fo*FaeC, Ser237, located in a position relevant to Arg411 of *Is*MHETase (Table S3), provides more space for the accommodation of longer ligands in the distal pocket of the active site, possibly explaining the ability of *Fo*FaeC WT to also act on BHET and other PET oligomers. Also, in *Fo*FaeC_G122S, the aromatic ring of Phe342, which overlaps with the Gln410 *Is*MHETase amide group, may enhance substrate selectivity toward longer phenolic compounds through potential π-π stacking interactions. Compared to Ser131 of *Is*MHETase, the hydroxyl group of engineered Ser122 in *Fo*FaeC_G122S is shifted to form a hydrogen bond with the alternative conformation of the catalytic Ser201 (Fig. 3B). Conversely, Ser131 in *Is*MHETase points toward the protein surface, where it is exposed to the solvent molecules (Fig. S8). A cross-substitution of hydrophobic residues occurs within the binding pockets of both enzymes (Fig. 3C), with Phe230 and Ile415 in *Fo*FaeC occupying positions equivalent to Leu254 and Phe495 in *Is*MHETase, respectively.

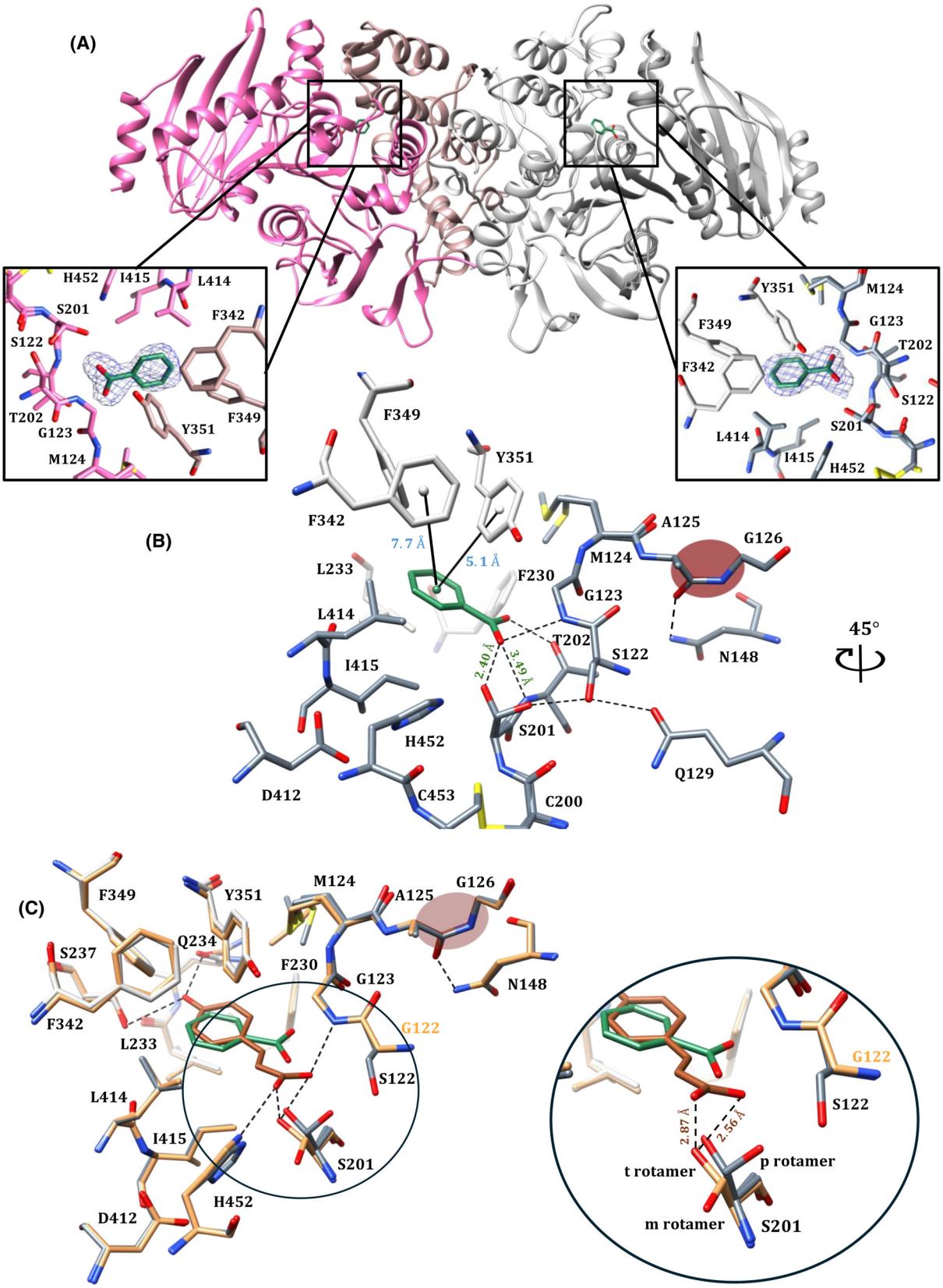
Molecular dynamics and docking simulations

MD simulations of apo structures

MD simulations with a total duration of 4 μs (2 systems × 4 trajectories × 500 ns) were used to estimate enzyme behavior before and after introducing mutation G122S. Both WT and MT are quite stable throughout the simulation, with an RMSD value of about 0.15 nm (Fig. S9). Additionally, thermostability analysis using the dimensionless parameter *Lambda* (Λ) indicated that the engineered mutation does not affect the overall thermostability of the enzyme, as the maximum distribution of both WT and MT occurs at the same Λ value (Fig. S10). This suggests that the

Fig. 2. Crystal structure of *Fo*FaeC_G122S in complex with benzoic acid. (A) Cartoon representation of both monomers in the a.u., highlighting the substrate binding site of *Fo*FaeC_G122S with benzoic acid modeled in both molecules (chain A in magenta/sandy brown and chain B in dark/light gray). Electron density maps are contoured at 1σ (blue mesh). Benzoic acid molecules are shown as dark green sticks. (B) Close-up view of the substrate binding site. The catalytic triad (Ser201-His452-Asp412) and the hydrophobic environment (Phe230, Leu233, Phe342, Phe349, Tyr351, Leu414, Ile415) are shown as sticks. The hydrogen bonds are shown in dashed black lines, while the distances between the centroids of Phe342/Tyr351 and BA are shown in continued black lines. (C) Superposition of *Fo*FaeC_G122S-BA and wild-type *Fo*FaeC-*p*CA with a close-up view of the binding pocket. The hydrogen bonds of *p*CA with its environment residues are shown in dashed black lines.

18733468, 2026, 18, Downloaded from https://febs.onlinelibrary.wiley.com/doi/10.1002/1873-3468.70322 by DESY - Zentralbibliothek, Wiley Online Library on [07/10/2026]. See the Terms and Conditions (https://onlinelibrary.wiley.com/terms-and-conditions) on Wiley Online Library for rules of use; OA articles are governed by the applicable Creative Commons License



18733468, 2026, 18, Downloaded from https://febs.onlinelibrary.wiley.com/doi/10.1002/1873-3468.70322 by DESY - Zentralbibliothek, Wiley Online Library on [07/10/2026]. See the Terms and Conditions (https://onlinelibrary.wiley.com/terms-and-conditions) on Wiley Online Library for rules of use; OA articles are governed by the applicable Creative Commons License

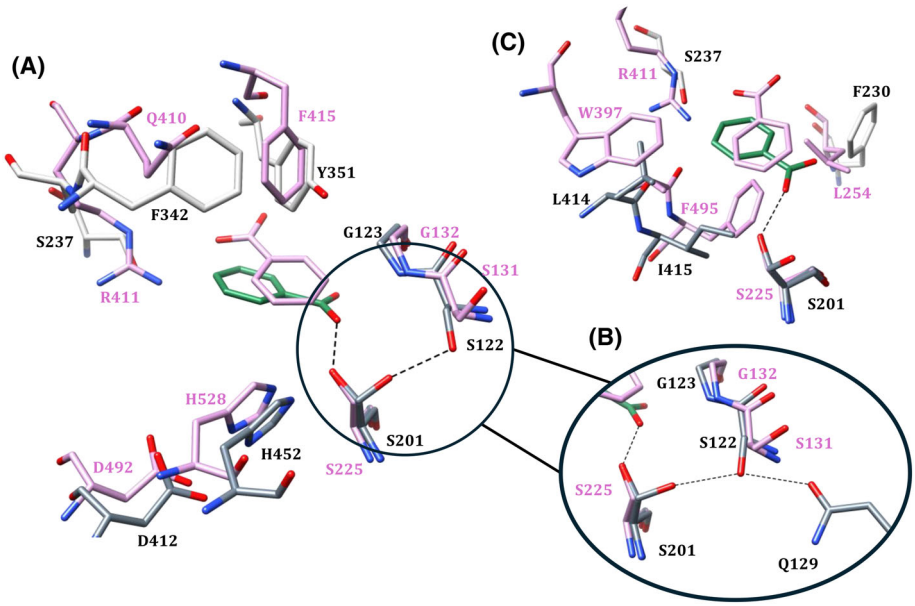


Fig. 3. Comparison of *Fo*FaeC_G122S and IsMHETase BA binding site. (A) Global view of the catalytic region of *Fo*FaeC_G122S (light/dark gray) and *Is*MHETase-6QZ3 (pink), in complex with BA. (B) Close-up view of engineered S122 and (C) hydrophobic cleft of binding pocket of the two enzymes.

backbone N-H vectors are temperature independent (within the temperature range probed), in agreement with the biochemical findings reported by *Makryniotis et al.* [10]. These authors showed that both WT and MT remain stable up to 45 °C, but undergo a sharp loss of activity at temperatures above 60 °C. A similar thermal behavior has been reported for *Is*MHETase, which is rapidly inactivated above 44 °C [6], as well as for Mle046, a rather psychrophilic MHETase-like enzyme identified in a marine microbial consortium [38].

The most important alterations apparently induced by G122S mutation are observed in regions 70–75, 96–100, 120–130, 142–179, and 295–306 (Fig. 4A, B, Fig. S11 and Fig. S12). With the exception of residues 70–75 (loop 3), which belong to the hydrolase domain and seem to become more flexible after the engineered mutation, all other amino acid groups appear to become less flexible. The region 120–130 (loop 6) contains the engineered mutation, and its increased stability is apparently due to the hydrogen bonds introduced by the hydroxyl group of Ser122. Reduced flexibility is also observed at Gly123 of the oxyanion hole of the binding pocket and at the peptide bond Ala125-Gly126, which adopts *trans*/*cis* conformation in the crystallographic MT structure. This region is located next to the catalytic serine, potentially contributing to substrate binding during catalysis. The enhanced stabilization of loop 7 (residues 142–179) is also associated with the *trans* to *cis* rearrangement, mediated by the hydrogen bond between Ala125 and Asn148 observed in the *cis* conformation. Last, loop 10 (residues 295–306) corresponds to a highly flexible loop on the upper part of the lid domain, evidenced from high B-factors relative to the rest of the structure, but also the absence of sufficient electron density in the crystallographic structure of *Fo*FaeC in complex with *p*CA acid (PDB code: 8BHH). The stabilization of this loop is also observed in the case of *Is*MHETase upon substrate binding [37]. Specifically, MD simulations of apo- and substrate-bound *Is*MHETase revealed a substrate-induced stabilization of loop 14 (residues 325–351 in *Is*MHETase, 288–307 (loop 10) in *Fo*FaeC) and loop 18 (residues 454–462 in *Is*MHETase). In *Fo*FaeC, the region corresponding to loop 18 of *Is*MHETase harbors an extended N-glycosylation from Asn362. Consistently, a distance-dependent stabilization is observed in *Fo*FaeC when the ΔRMSF values (RMSF of MT minus WT) are considered relative to the Cα – Cα distance from Ser122 (Fig. 4C), with residues closer to the mutation site exhibiting reduced flexibility (ΔRMSF < 0) and more distant residues displaying progressively smaller differences. Notably, reduced flexibility is also observed for loop 10, suggesting that the G122S mutation may influence long-range dynamic properties of the protein.

18733468, 2026, 18, Downloaded from https://febs.onlinelibrary.wiley.com/doi/10.1002/1873-3468.70322 by DESY - Zentralbibliothek, Wiley Online Library on [07/10/2026]. See the Terms and Conditions (https://onlinelibrary.wiley.com/terms-and-conditions) on Wiley Online Library for rules of use; OA articles are governed by the applicable Creative Commons License

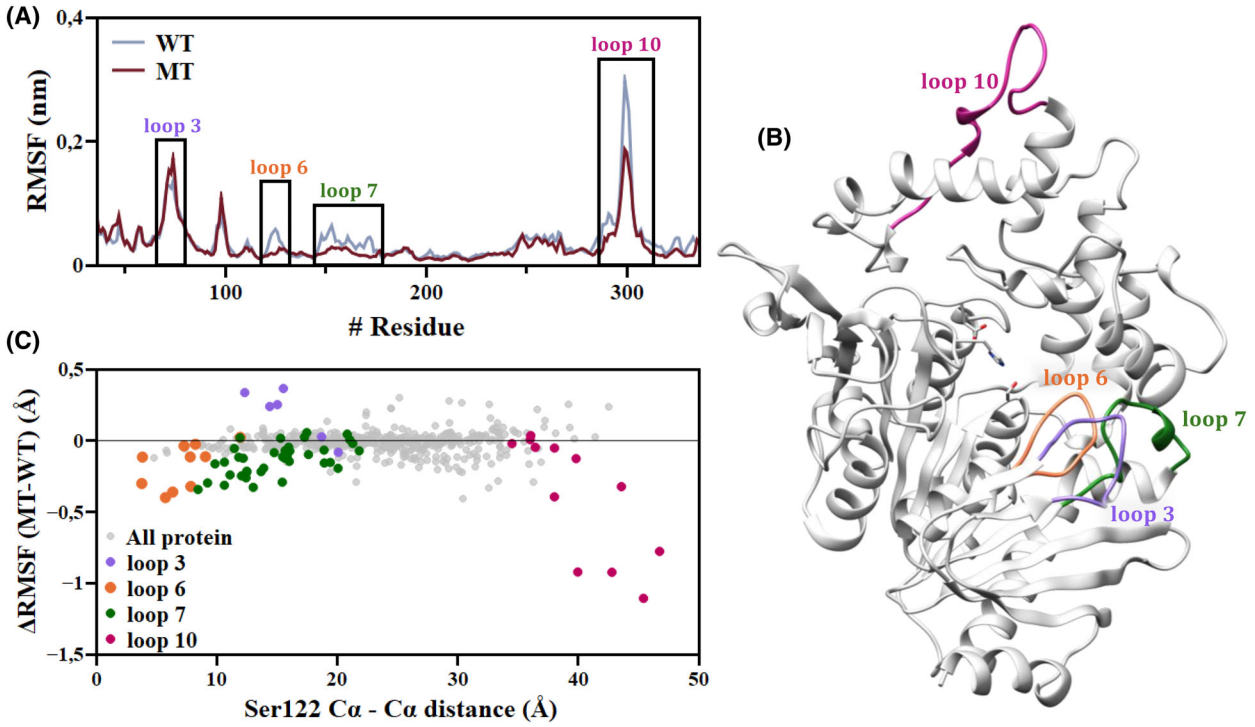


Fig. 4. RMSF profiles of WT and MT *Fo*FaeC over 500 ns MD simulation. (A) RMSF profiles of WT (light blue) and MT (dark red) *Fo*FaeC. Loops 3, 6, 7, and 10 are highlighted in purple, orange, green, and magenta, respectively. The full RMSF plot including all residues (36–543) is provided in Fig. S12. (B) Cartoon representation of *Fo*FaeC with the same loop color scheme. The catalytic triad (Ser201 – His452 – Asp412) is depicted as light gray sticks and colored by heteroatoms (oxygen – red, nitrogen—blue). (C) Difference in RMSF (MT – WT) as a function of the Cα – Cα distance from the mutated residue Ser122, with data points colored according to the corresponding loops.

Docking and MD simulations

Molecular docking of *Fo*FaeC and *Fo*FaeC_G122S with MHET was performed to further examine the role of the engineered residue in the increased activity of the enzyme against MHET. Principal component analysis on the motion of the binding pocket residues followed by k-means clustering resulted in four distinct configurations per enzyme. The binding free energy of the two complexes selected for MD was calculated to be 5.34 kcal·mol^{-1} and 5.36 kcal·mol^{-1} for *Fo*FaeC and *Fo*FaeC_G122S, respectively, while the dissociation constant for each complex was 0.10 mM and 0.12 mM at 273 K, respectively. The MHET molecule was similarly positioned in both cases, with its aromatic ring being accommodated in the hydrophobic cavity composed of Ile415, Leu414, Phe342 and 349, as well as Tyr351, and its ethylene glycol moiety pointing toward the solvent exposed side of the protein (Fig. 5A). A similar orientation is observed in the MHETA bound structure of *Is*MHETase (PDB code: 6QGA, Fig. 5B). The docked MHET molecule forms hydrogen bonds with catalytic residues Ser201 and His452, as well as with the residues Gly123, Leu233, Gln234, Ser237, Phe349, Leu414, and Ile415 of the binding pocket. In *Fo*FaeC_G122S, MHET additionally forms hydrogen bonds with residues Thr75, Ser122, Met124, Ala227, Phe342, and Tyr351, while in *Fo*FaeC, with residues Thr202 and Cys543.

The selected structures (WT and MT in complex with MHET) were equilibrated and subjected to MD dynamics yielding four independent trajectories each, following the same procedure used for the apo structures, increasing the cumulative simulation time for the current study to 8 μs. The *Fo*FaeC and *Fo*FaeC_G122S complexes showed an RMSD value of 0.18 nm and 0.14 nm, respectively, while the RMSD calculated for the carbon atoms of the aromatic ring of the MHET moiety remained low at 0.01 nm (Fig. S13). The RMSF analysis of the proteins revealed that loops 6 (the engineered mutation region) and 7 display increased flexibility in the MT complex compared to the apo form, whereas the flexibility of the corresponding loops in the WT remained almost unchanged upon MHET binding (Fig. 6A,C, Fig. S14).

During the simulations of the complex structures, the side chain of Phe342 adopts the closed

18733468, 2026, 18, Downloaded from https://febs.onlinelibrary.wiley.com/doi/10.1002/1873-3468.70322 by DESY - Zentralbibliothek, Wiley Online Library on [07/10/2026]. See the Terms and Conditions (https://onlinelibrary.wiley.com/terms-and-conditions) on Wiley Online Library for rules of use; OA articles are governed by the applicable Creative Commons License

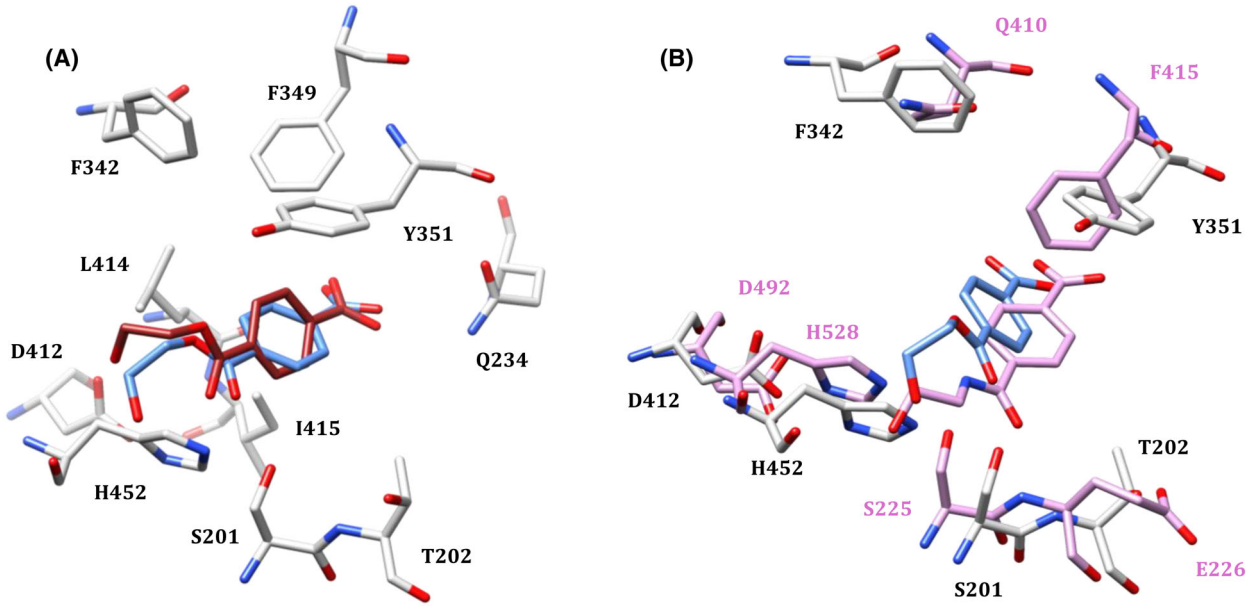


Fig. 5. Molecular docking analysis illustrates MHET binding within the active site of *Fo*FaeC. (A) Superposition of WT (blue) and MT (red) *Fo*FaeC structures after docking simulations with MHET. (B) Superposition of WT *Fo*FaeC (light gray) in complex with MHET (blue) and *Is*MHETase in complex with MHETA (purple). Residues are shown in stick representation and colored by heteroatoms (oxygen—red, nitrogen—blue).

conformation, while Tyr351 exhibited enhanced mobility, forming π-π stacking interactions with the phenolic moiety of the ligand. The observed mobility of Tyr351, as well as the closed conformation of Phe342 in ligand-bound structures, agrees with the crystallographic observation from the *Fo*FaeC_G122S-BA and *Fo*FaeC-*p*CA complex structures. Analysis of the distance between the Cα atoms of His452 (hydrolase domain, catalytic residue) and Phe342 (lid domain) showed that the MT exhibits a broader distance distribution in the unbound state (Fig. 6D), indicating increased relative motion between the hydrolase and lid domains.

In addition to the RMSF analysis, the radius of gyration of the binding pocket was examined for both apo and MHET bound states for WT and MT *Fo*FaeC. The pocket was defined based on the backbone atoms (N – Cα – C) of the catalytic residues Ser201, His452, Asp412, as well as residues involved in ligand binding, including the engineered Ser122. These residues include Ser122/Gly122, Gly123, Met124, Thr202, Phe230, Leu233, Gln234, Ser237, Phe342, Phe349, Tyr351, Leu414, and Ile415 (Fig. S15). The analysis revealed a noticeably enlarged substrate binding cavity for MT, showing an approximately 2 Å increase in pocket size upon MHET binding (Fig. 6E). This expansion suggests that the MT binding pocket can accommodate larger substrates, in agreement with the biochemically observed promiscuity of the enzyme [10].

Conclusions

The efficient degradation of PET by the plastic-degrading bacterium *Ideonella sakaiensis* 201-F6 requires the synergistic effect of PETase and MHETase, highlighting the necessity of the latter for efficient plastic degradation to its monomers and subsequent upcycling. One important drawback that has to be tackled before microbe-free enzyme-mediated depolymerization, is substrate inhibition that is observed in MHETase, which was alleviated by introducing the S131G mutation in *Is*MHETase, which however also reduced reaction efficiency [5]. Here, we present a structural analysis of the 'reverse mutant' in *Fo*FaeC, where the corresponding Gly122 was mutated to Ser, resulting in a more efficient and promiscuous enzyme variant.

Despite cocrystallizing *Fo*FaeC_G122S with MHET, clear electron density next to the catalytic serine indicated the presence of BA. The crystal structure of *Is*MHETase in complex with BA has also been previously reported [5,6], and however, it is not clear whether these structures are derived from crystals

18733468, 2026, 18, Downloaded from https://febs.onlinelibrary.wiley.com/doi/10.1002/1873-3468.70322 by DESY - Zentralbibliothek, Wiley Online Library on [07/10/2026]. See the Terms and Conditions (https://onlinelibrary.wiley.com/terms-and-conditions) on Wiley Online Library for rules of use; OA articles are governed by the applicable Creative Commons License

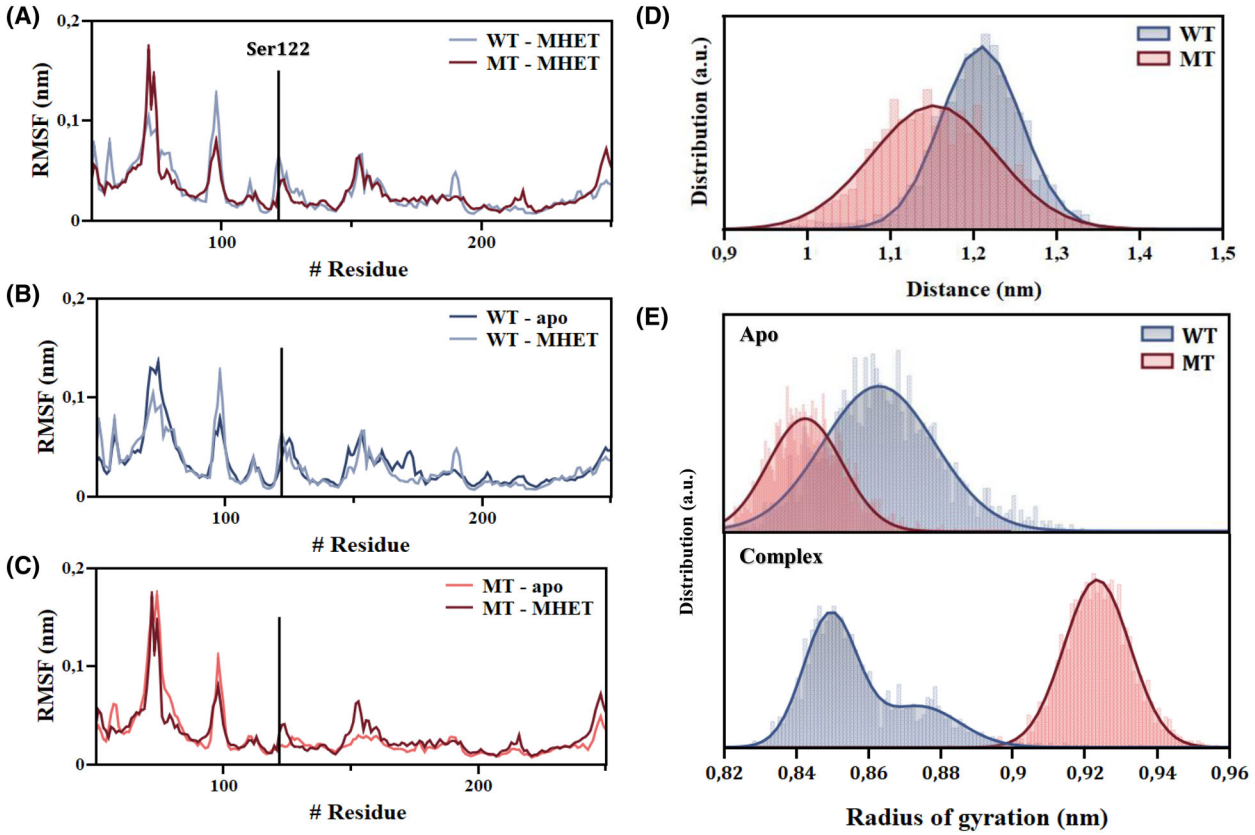


Fig. 6. MD analysis. (A) RMSF profiles of WT and MT *Fo*FaeC in complex with MHET. (B) and (C) Comparison of RMSF profiles of apo and MHET bound forms in WT and MT, respectively. (D) Histogram of the distance between Cα atoms of His452 and Phe342, residues of the hydrolase and lid domains, respectively. Distances are calculated for the apo structures. (E) Histograms of the radius of gyration of the binding pocket for WT and MT *Fo*FaeC, comparing the apo and MHET bound states.

soaked or cocrystallized with BA. One explanation for the observation of benzoic instead of MHET in the *Fo*FaeC_G122S active site could be radiation damage during X-ray data collection [39].

The analysis of the biochemical characteristics of *Fo*FaeC_G122S revealed a more promiscuous enzyme, capable of catalyzing the breakage of a greater variety of natural and synthetic esters [10]. The crystal structure of *Fo*FaeC_G122S in apo state reveals a twisted *trans* conformation in the peptide bond between amino acids 125 and 126 in monomer A, and a *cis* conformation in monomer B. Also, interestingly, and in contrast to the WT-apo enzyme, such transition to *cis* peptide is also observed in the *p*CA acid bound structure of *Fo*FaeC WT (PDB code: 8BHH) and the BA bound structure of *Fo*FaeC_G122S. In parallel, MD simulations reveal that the engineered mutation results in a less flexible loop L6, which is the loop that harbors the aforementioned amino acids, as well as loop 10, which has been shown to be stabilized upon MHET binding in *Is*MHETase. Gly126 is a conserved amino acid among *Fo*FaeC homologs (Fig. S16). Given the inherent flexibility of glycine and its ability to accommodate backbone conformational changes, its conservation suggests a structural role in modulating the geometry required for substrate binding. The implication of this region to substrate stabilization has been recently also demonstrated in the computational work by *Wang et al* [37]. Additionally, Phe342 is found in two distinct conformations in the determined crystal structures, an open state which is combined with a *trans* conformation of 125–126 bond and a closed one, found in complex structures, and combined with the *cis* conformation observed in the 125–126 peptide bond. It could thus be suggested that the introduced mutation favors a structural rearrangement of the enzyme's active site to resemble the ligand-bound state, involving the movement of Phe342 acid chain and *cis-trans* alteration of the 125–126 peptide bond and the stabilization of loops 6 and 10. The implication of this *cis-trans* variation in ligand binding has been shown in previous studies [40] and suggested to

18733468, 2026, 18, Downloaded from https://febs.onlinelibrary.wiley.com/doi/10.1002/1873-3468.70322 by DESY - Zentralbibliothek, Wiley Online Library on [07/10/2026]. See the Terms and Conditions (https://onlinelibrary.wiley.com/terms-and-conditions) on Wiley Online Library for rules of use; OA articles are governed by the applicable Creative Commons License

be related to enzyme evolution for new substrates and functions. The role of Gln410 of *Is*MHETase, located at a position corresponding to Phe342, has been shown in the work by *Knott et al* [5], who suggested a concerted movement of Phe415 that adopts an open and close conformation, and Gln410 upon substrate binding. Similarly, Tyr351 of *Fo*FaeC, which occupies a position analogous to Phe415 of *Is*MHETase, has been reported in previous X-ray crystallographic studies to exhibit high mobility and to contribute to substrate binding through the formation of π-π stacking interactions with the aromatic rings of the substrates [9].

In summary, the introduced mutation yields a variant with broadened substrate scope, driven by the formation of novel intramolecular interactions, loop stabilization, and expansion of the binding cavity. This study advances our understanding of the structural determinants underlying increased enzyme promiscuity in an MHET-active esterase. The insights obtained provide a foundation for future enzyme-engineering strategies aimed at developing robust biocatalysts for a wide range of biotechnological applications, including plastic biodegradation. Moreover, in an era of rapidly advancing computational structure prediction, this work underscores the value of integrating experimental and computational approaches, particularly for validating the structural and functional consequences of point mutations.

Author contributions

MD and ET conceptualization. MD and VD methodology. PK, TIS, MD, and VD data curation and formal analysis. PK and KM performed the experiments. PK and MD writing original draft. PK, KM, ET, VD, and MD writing – review and editing. MD, ET, and VD funding acquisition. MD and VD supervision.

Acknowledgements

This research was funded by the Hellenic Foundation for Research and Innovation (H.F.R.I.) under the 'Basic Research Funding (Horizontal support for all Sciences), National Recovery and Resilience Plan (Greece 2.0)—Sub-action II Funding Projects in Leading-Edge Sectors' (EnZyReMix, project number: 15024). The synchrotron data was collected at beamline P13 operated by EMBL Hamburg at the PETRA III storage ring (DESY, Hamburg, Germany). We would like to thank Dr. Isabel Bento for the assistance in using the beamline. This work was also supported by computational time granted from the National Infrastructures for Research and Technology S.A. (GRNET S.A.) in the National HPC facility—ARIS—under project ID 'MultiEng'. The publication of this article in OA mode was financially supported by HEAL-Link.

Peer review

The peer review history for this article is available at https://www.webofscience.com/api/gateway/wos/peer-review/10.1002/1873-3468.70322.

Data accessibility

The atomic coordinates of the three-dimensional structures presented in this work have been deposited in the Protein Data Bank (PDB) with PDB IDs: 9I50 and 9HUN. MD data are available upon reasonable requests from the corresponding author.

References

1 Yoshida S, Hiraga K, Takehana T, Taniguchi I, Yamaji H, Maeda Y, Toyohara K, Miyamoto K, Kimura Y and Oda K (2016) A bacterium that degrades and assimilates poly(ethylene terephthalate). *Science* **351**, 1196–1199. doi: 10.1126/science.aad6359

2 Groseclose TM and Nguyen HB (2025) Recent advances in enzyme engineering for improved deconstruction of poly(ethylene terephthalate) (PET) plastics. *Commun Mater* **6**, 190. doi: 10.1038/s43246-025-00919-8

3 Underlin EN, Frommhagen M, Dilokpimol A, van Erven G, de Vries RP and Kabel MA (2020) Feruloyl Esterases for biorefineries: subfamily classified specificity for natural substrates. *Front Bioeng Biotechnol* **8**, doi: 10.3389/fbioe.2020.00332

4 Sagong H-Y, Seo H, Kim T, Son HF, Joo S, Lee SH, Kim S, Woo JS, Hwang SY and Kim KJ (2020) Decomposition of the PET film by MHETase using Exo-PETase function. *ACS Catal* **10**, 4805–4812. doi: 10.1021/acscatal.9b05604

5 Knott BC, Erickson E, Allen MD, Gado JE, Graham R, Kearns FL, Pardo I, Topuzlu E, Anderson JJ, Austin HP *et al.* (2020) Characterization and engineering of a two-enzyme system for plastics depolymerization. *Proc Natl Acad Sci* **117**, 25476–25485. doi: 10.1073/pnas.2006753117

6 Palm GJ, Reisky L, Böttcher D, Müller H, Michels EAP, Walczak MC, Berndt L, Weiss MS, Bornscheuer UT and Weber G (2019) Structure of the plastic-degrading Ideonella sakaiensis MHETase bound to a substrate. *Nat Commun* **10**, 1717. doi: 10.1038/s41467-019-09326-3

18733468, 2026, 18, Downloaded from https://febs.onlinelibrary.wiley.com/doi/10.1002/1873-3468.70322 by DESY - Zentralbibliothek, Wiley Online Library on [07/10/2026]. See the Terms and Conditions (https://onlinelibrary.wiley.com/terms-and-conditions) on Wiley Online Library for rules of use; OA articles are governed by the applicable Creative Commons License

7 Saunders JW, Damry AM, Vongsouthi V, Spence MA, Frkic RL, Gomez C, Yates PA, Matthews DS, Tokuriki N, McLeod MD *et al.* (2024) Increasing the soluble expression and whole-cell activity of the plastic-degrading enzyme MHETase through consensus design. *Biochemistry* **63**, 1663–1673. doi: 10.1021/acs.biochem.4c00165
8 Dimarogona M, Topakas E, Christakopoulos P and Chrysina ED (2020) The crystal structure of a fusarium oxysporum feruloyl esterase that belongs to the tannase family. *FEBS Lett* **594**, 1738–1749. doi: 10.1002/1873-3468.13776
9 Ferousi C, Kosinas C, Nikolaivits E, Topakas E and Dimarogona M (2023) Crystal structure of the fusarium oxysporum tannase-like feruloyl esterase FaeC in complex with p-coumaric acid provides insight into ligand binding. *FEBS Lett* **597**, 1415–1427. doi: 10.1002/1873-3468.14615
10 Makryniotis K, Papi M, Nikolaivits E and Topakas E (2025) Structure-guided engineering of a fungal feruloyl esterase enhances both MHET conversion and lignocellulose breakdown. *Int J Biol Macromol* **333**, 148892. doi: 10.1016/j.ijbiomac.2025.148892
11 Cianci M, Bourenkov G, Pompidor G, Karpics I, Kallio J, Bento I, Roessle M, Cipriani F, Fiedler S and Schneider TR (2017) P13, the EMBL macromolecular crystallography beamline at the low-emittance PETRA III ring for high- and low-energy phasing with variable beam focusing. *J Synchrotron Radiat* **24**, 323–332. doi: 10.1107/S1600577516016465
12 Kabsch W (2010) XDS. *Acta Crystallogr D Biol Crystallogr* **66**, 125–132. doi: 10.1107/S0907444909047337
13 Evans PR (2011) An introduction to data reduction: space-group determination, scaling and intensity statistics. *Acta Crystallogr D Biol Crystallogr* **67**, 282–292. doi: 10.1107/S090744491003982X
14 Winn MD, Ballard CC, Cowtan KD, Dodson EJ, Emsley P, Evans PR, Keegan RM, Krissinel EB, Leslie AGW, McCoy A *et al.* (2011) Overview of the CCP4 suite and current developments. *Acta Crystallogr D Biol Crystallogr* **67**, 235–242. doi: 10.1107/S0907444910045749
15 McCoy AJ, Grosse-Kunstleve RW, Adams PD, Winn MD, Storoni LC and Read RJ (2007) Phaser crystallographic software. *J Appl Crystallogr* **40**, 658–674. doi: 10.1107/S0021889807021206
16 Emsley P and Cowtan K (2004) Coot: model-building tools for molecular graphics. *Acta Crystallogr D Biol Crystallogr* **60**, 2126–2132. doi: 10.1107/S0907444904019158
17 Murshudov GN, Vagin AA and Dodson EJ (1997) Refinement of macromolecular structures by the maximum-likelihood method. *Acta Crystallogr D Biol Crystallogr* **53**, 240–255. doi: 10.1107/S0907444996012255
18 Olsson MHM, Søndergaard CR, Rostkowski M and Jensen JH (2011) PROPKA3: consistent treatment of internal and surface residues in empirical pKa predictions. *J Chem Theory Comput* **7**, 525–537. doi: 10.1021/ct100578z
19 Søndergaard CR, Olsson MHM, Rostkowski M and Jensen JH (2011) Improved treatment of ligands and coupling effects in empirical calculation and rationalization of pKa values. *J Chem Theory Comput* **7**, 2284–2295. doi: 10.1021/ct200133y
20 Moukouli M, Topakas E and Christakopoulos P (2008) Cloning, characterization and functional expression of an alkalitolerant type C feruloyl esterase from fusarium oxysporum. *Appl Microbiol Biotechnol* **79**, 245–254. doi: 10.1007/s00253-008-1432-3
21 "Structure and dynamics of the TIP3P, SPC, and SPC/E water models at 298 K | the journal of physical chemistry A." Accessed: Jan. 20, 2025. [Online]. Available: https://pubs.acs.org/doi/10.1021/jp003020w
22 "Implementation of the CHARMM force field in GROMACS: analysis of protein stability effects from correction maps, virtual interaction sites, and water models | journal of chemical theory and computation." Accessed: Jan. 20, 2025. [Online]. Available: https://pubs.acs.org/doi/10.1021/ct900549r
23 "Structure and dynamics of a thermostable alcohol dehydrogenase from the antarctic psychrophile moraxella sp. TAE123 | ACS Omega." Accessed: Jan. 21, 2025. [Online]. Available: https://pubs.acs.org/doi/10.1021/acsomega.0c01210
24 Berendsen HJC, van der Spoel D and van Drunen R (1995) GROMACS: a message-passing parallel molecular dynamics implementation. *Comput Phys Commun* **91**, 43–56. doi: 10.1016/0010-4655(95)00042-e
25 Darden T, York D and Pedersen L (1993) Particle mesh Ewald: an N·log(N) method for Ewald sums in large systems. *J Chem Phys* **98**, 10089–10092. doi: 10.1063/1.464397
26 Hess B, Bekker H, Berendsen HJC and Fraaije JGEM (1997) LINCS: a linear constraint solver for molecular simulations. *J Comput Chem* **18**, 1463–1472. doi: 10.1002/(SICI)1096-987X(199709)18:12<1463::AID-JCC4>3.0.CO;2-H
27 Bussi G, Donadio D and Parrinello M (2007) Canonical sampling through velocity rescaling. *J Chem Phys* **126**, 014101. doi: 10.1063/1.2408420
28 Bernetti M and Bussi G (2020) Pressure control using stochastic cell rescaling. *J Chem Phys* **153**, 114107. doi: 10.1063/5.0020514
29 Land H and Humble MS (2018) YASARA: a tool to obtain structural guidance in biocatalytic investigations. In Protein Engineering: Methods and Protocols

18733468, 2026, 18, Downloaded from https://febs.onlinelibrary.wiley.com/doi/10.1002/1873-3468.70322 by DESY - Zentralbibliothek, Wiley Online Library on [07/10/2026]. See the Terms and Conditions (https://onlinelibrary.wiley.com/terms-and-conditions) on Wiley Online Library for rules of use; OA articles are governed by the applicable Creative Commons License

(Bornscheuer UT and Höhne M, eds), pp. 43–67. Springer, New York, NY. doi: 10.1007/978-1-4939-7366-8_4
30 Konagurthu AS, Whisstock JC, Stuckey PJ and Lesk AM (2006) MUSTANG: a multiple structural alignment algorithm. *Proteins Struct Funct Bioinform* **64**, 559–574. doi: 10.1002/prot.20921
31 Jo S, Kim T, Iyer VG and Im W (2008) CHARMM-GUI: a web-based graphical user interface for CHARMM. *J Comput Chem* **29**, 1859–1865. doi: 10.1002/jcc.20945
32 Kim S, Lee J, Jo S, Brooks CL III, Lee HS and Im W (2017) CHARMM-GUI ligand reader and modeler for CHARMM force field generation of small molecules. *J Comput Chem* **38**, 1879–1886. doi: 10.1002/jcc.24829
33 Zeiske T, Stafford KA and Palmer AGI (2016) Thermostability of enzymes from molecular dynamics simulations. *J Chem Theory Comput* **12**, 2489–2492. doi: 10.1021/acs.jctc.6b00120
34 Daskalakis V and Papapetros S (2024) Engineering salt-tolerant Cas12f1 variants for gene-editing applications. *J Biomol Struct Dyn* **42**, 7421–7431. doi: 10.1080/07391102.2023.2240418
35 Lovell SC, Word JM, Richardson JS and Richardson DC (2000) The penultimate rotamer library. *Proteins Struct Funct Bioinforma* **40**, 389–408. doi: 10.1002/1097-0134(20000815)40:3<389::AID-PROT50>3.0.CO;2-2
36 Piovesan D, Minervini G and Tosatto SCE (2016) The RING 2.0 web server for high quality residue interaction networks. *Nucleic Acids Res* **44**, W367–W374. doi: 10.1093/nar/gkw315
37 Wang D, Yang M, Zhang Z, Zhao Y, Lyu C, Qiu S, Mei L, Fan F and Huang J (2025) Substrate recognition and dynamic transport in MHETase reveal the regulation mechanism of gatekeeper residues: a theoretical investigation. *Phys Chem Chem Phys* **27**, 22448–22463. doi: 10.1039/D5CP03204K
38 Meyer-Cifuentes IE and Öztürk B (2021) Mle046 is a marine mesophilic MHETase-like enzyme. *Front Microbiol* **12**, doi: 10.3389/fmicb.2021.693985
39 Jamalzadeh M and Sobkowicz MJ (2022) Review of the effects of irradiation treatments on poly(ethylene terephthalate). *Polym Degrad Stab* **206**, 110191. doi: 10.1016/j.polymdegradstab.2022.110191
40 Joseph AP, Srinivasan N and de Brevern AG (2012) Cis–trans peptide variations in structurally similar proteins. *Amino Acids* **43**, 1369–1381. doi: 10.1007/s00726-011-1211-9

Supporting information

Additional supporting information may be found online in the Supporting Information section at the end of the article.

Fig. S1. Superposition of *Fo*FaeC and *Is*MHETase (PDB code: 6FAT and 6JTT, respectively) resulting in an RMSD value of 1.953 Å. *Fo*FaeC is depicted in orange cartoon representation, whereas *Is*MHETase is shown in green.
Fig. S2. SDS-PAGE gel (12.5%w/w) of purified *Fo*FaeC_G122S.
Fig. S3. *Fo*FaeC_G122S crystals grown in the presence of 0.1 M Tris–HCl pH 8.5 and 35% (v/v) PEG400. The size of the crystals was measured using ImageJ online program (https://imagej.net/ij/).
Table S1. Data collection and processing statistics.
Table S2. Structure solution and refinement.
Fig. S4. Total K-means clustering of the four independent WT trajectories over 500 ns MD simulation.
Fig. S5. Total K-means clustering of the four independent MT trajectories over 500 ns MD simulation.
Fig. S6. Representation of the crystal structure of *Fo*FaeC_G122S, chain B (PDB ID: 9I50) in COOT. Amino acids are shown in stick models colored by heteroatoms. The $2F_o - F_c$ electron density map is contoured at 1σ (blue mesh), while the $F_o - F_c$ difference map is contoured at 3σ (green mesh).
Fig. S7. Representation of the crystal structure of *Fo*FaeC_G122S, chain B (PDB ID: 9I50) in COOT. Close-up view of Tyr351 highlighting its mobility due to the non-satisfied electron density map around it. Amino acids are shown in stick models colored by heteroatoms. The $2F_o - F_c$ electron density map is contoured at 1σ (blue mesh), while the $F_o - F_c$ difference map is contoured at 3σ (green mesh).
Fig. S8. Surface representation of the cavity around hydroxyl group of Ser131 in *Is*MHETase (PDB code 9QZ3) and engineered Ser122 in *Fo*FaeC_G122S-BA. *Is*MHETase is shown in pink color, while *Fo*FaeC_G122S is in gray colors. Ser131 of *Is*MHETase interacts with water molecules, while Ser122 in *Fo*FaeC_G122S-BA forms hydrogen bonds with Gln129 and catalytic Ser201.
Table S3. Residues implicated in catalysis and substrate binding, in *Fo*FaeC and *Is*MHETase. Those belonging to the lid domain are shown in red, while those from the catalytic domain in blue.
Fig. S9. Root Mean Square Deviation (RMSD) profiles of *Fo*FaeC over 500 ns of molecular dynamics simulation. The wild-type (WT) *Fo*FaeC is shown in blue, while the mutant (MT) *Fo*FaeC_G122S is in red.
Fig. S10. Histogram of Λ values for the wild-type and mutant G122S for the whole enzymes. A solid line guide (Gaussian fitting) is provided for each histogram to determine the Λ value of the maximum distribution of each enzyme. Lower Λ values indicate higher protein thermostability.

18733468, 2026, 18, Downloaded from https://febs.onlinelibrary.wiley.com/doi/10.1002/1873-3468.70322 by DESY - Zentralbibliothek, Wiley Online Library on [07/10/2026]. See the Terms and Conditions (https://onlinelibrary.wiley.com/terms-and-conditions) on Wiley Online Library for rules of use; OA articles are governed by the applicable Creative Commons License

Fig. S11. Secondary structure elements correspond to *Fo*FaeC_G122S, highlighting loops (L) regions (L1-20). It also shows the α-helices and β-strands. The figure was prepared using ESPRIPT (https://espript.ibcp.fr/ESPript/ESPript/).

Fig. S12. Root Mean Square Fluctuation (RMSF) profiles of FoFaeC over 500 ns molecular dynamics simulation. The wild-type (WT) *Fo*FaeC is shown in blue, while the mutant (MT) FoFaeC_G122S is in dark red.

Fig. S13. RMSD profiles of *Fo*FaeC (A) and violin plots of the RMSD for the aromatic ring of MHET (B) over 500 ns of molecular dynamics simulation. The wild-type (WT) *Fo*FaeC is shown in blue, while the mutant (MT) *Fo*FaeC_G122S is in red.

Fig. S14. Root Mean Square Fluctuation (RMSF) profiles of *Fo*FaeC in complex with MHET over 500 ns molecular dynamics simulation. The wild-type (WT) *Fo*FaeC is shown in blue, while the mutant (MT) *Fo*FaeC_G122S is in dark red.

Fig. S15. Residues forming the binding pocket in MT and used for the R_g calculation are shown in pink stick representation.

Fig. S16. A BLAST search against UniProtKB/Swiss-Prot database was performed using the *Fo*FaeC_G122S sequence as input. To identify evolutionary conserved regions, the BLAST output FAE sequences were aligned with *Fo*FaeC_G122S, revealing that Gly126 is highly conserved among the homologous proteins (red arrow). The figure was prepared using ESPRIPT (https://espript.ibcp.fr/ESPript/ESPript/).

18733468, 2026, 18, Downloaded from https://febs.onlinelibrary.wiley.com/doi/10.1002/1873-3468.70322 by DESY - Zentralbibliothek, Wiley Online Library on [07/10/2026]. See the Terms and Conditions (https://onlinelibrary.wiley.com/terms-and-conditions) on Wiley Online Library for rules of use; OA articles are governed by the applicable Creative Commons License